



# Modulation of the Madden–Julian oscillation on the energetics of wintertime synoptic-scale disturbances

Lu Wang<sup>1,2</sup> · Tim Li<sup>1,2</sup> · Lin Chen<sup>1,2</sup>

Received: 8 January 2018 / Accepted: 25 August 2018 / Published online: 19 September 2018  
© Springer-Verlag GmbH Germany, part of Springer Nature 2018

## Abstract

Numerous studies have devoted to energetic balance diagnosis of the synoptic scale disturbance (SSD) in the northern summer monsoon region, but few work has concentrated on that during boreal winter. This study investigated the energetics of the SSD associated with the eastward propagating Madden–Julian oscillation (MJO) convection south of the equator during boreal winter. The eddy kinetic energy is enhanced within and to the west of the MJO convection and is weakened to the east of it. This is related to the barotropic energy conversion (CK) in lower and middle troposphere and conversion of eddy available potential energy (CA) in upper troposphere. CK arises from interactions between SSD and MJO/lower-frequency flows. The SSD in the vicinity of the MJO is characterized by a wavelike pattern, with northwest to southeast tilt of elongated extrema of vorticity anomalies. The MJO flow in lower troposphere is characterized by zonal convergence at the convection center and cyclonic (anticyclonic) circulation to the east (west). The lower-frequency background flow is cyclonically sheared in the southern Indian Ocean. More (less) CA to the west (east) is due to more (less) generated eddy available potential energy from diabatic effects. The SSD contribute to the MJO eastward propagation through inducing a zonal asymmetry in nonlinear moisture advective tendency. This accounts for 30% of the observed asymmetric intraseasonal moisture tendency.

## 1 Introduction

Vigorous tropical synoptic-scale disturbances (SSDs) have been shown to be important for many climate phenomena (e.g., Lau and Lau 1990; Liu and Wang 2012; Li 2014). Some of them serve as “seeds” for genesis of tropical cyclones (e.g., Bracken and Bosart 2000; Zhou and Wang 2007). Some of them are linked to “westerly wind burst” over the western-central Pacific, which is considered important for the initiation of an El Niño event (e.g., McPhaden

2004; Seiki and Takayabu 2007; Chen et al. 2017). It has been reported that the SSDs are highly dependent on the state of large scale atmospheric circulation (e.g., Sui and Lau 1992; Li et al. 2013; Wang and Chen 2016, 2017). Therefore, understanding the interactions between SSDs and the large-scale circulation maybe helpful to predict some climate phenomena (e.g., Liu et al. 2015).

Numerous studies have been devoted to investigate the relationship between the tropical SSDs and large scale circulation during boreal summer (e.g., Reed and Recker 1971; Lau and Lau 1990, 1992; Chang et al. 1996; Sobel and Bretherton 1999; Li 2006). The most active regions for SSDs are in the northern hemisphere, especially where the background mean flow is cyclonic and convergent. The typical structure of the SSDs in northern tropical region is characterized by a wavelike pattern with a southwest to northeast tilt of elongated extrema of vorticity anomalies, moving westward or northwestward. Eddy kinetic energy budget analysis indicates that the primary energy source for the SSDs is the conversion from the eddy available potential energy in upper troposphere, while the barotropic energy conversion from environmental flows also play a substantial role especially in lower troposphere.

✉ Lu Wang  
luwang@nuist.edu.cn

✉ Tim Li  
timli@hawaii.edu

<sup>1</sup> Key Laboratory of Meteorological Disaster, Ministry of Education (KLME)/Joint International Research Laboratory of Climate and Environmental Change (ILCEC)/ Collaborative Innovation Center on Forecast and Evaluation of Meteorological Disasters (CIC-FEMD), Nanjing University of Information Science and Technology, Nanjing, China

<sup>2</sup> International Pacific Research Center, and School of Ocean and Earth Science and Technology, University of Hawaii, Honolulu, HI, USA

Since the boreal summer intraseasonal oscillation (ISO) could strongly impact the variations in the large-scale flow, the SSD activities vary in different ISO phases (e.g., Straub and Kiladis 2003; Maloney and Hartmann 2001; Maloney and Dickinson 2003). For instance, the SSD over the western North Pacific (WNP) is more vigorous during the ISO westerly phase, when a cyclonic circulation anomaly is generated over the WNP in response to an enhanced ISO convection at the equatorial western Pacific. And the SSD is less vigorous during the ISO easterly phase, when an anticyclonic circulation anomaly is generated over the WNP in response to a suppressed ISO convection at the equatorial western Pacific. The enhanced (suppressed) SSD activity coincides with the increase (decrease) of barotropic conversion from environmental flow, and this has been attributed to the intensified (weakened) monsoon trough over the WNP.

Recently, Hsu et al. (2011) developed an energetic tool which could separate the effect of the ISO flow and the lower-frequency background flow on barotropic conversion. Their diagnosis suggested that the barotropic conversion anomalies over the WNP shown in different ISO phases are caused by the ISO flows, which are cyclonic and convergent (anticyclonic and divergent) during the ISO westerly (easterly) phase. By contrast, the lower-frequency background flow always contributes positively toward the eddy kinetic energy regardless of ISO phases.

While most previous studies concentrated on the energetics of the SSDs during boreal summer, there are few works addressing the eddy energetics during boreal winter. As we know, the Madden–Julian oscillation (MJO) is most prominent during boreal winter and exhibits an eastward propagation especially in the southern equatorial Indian Ocean and western Pacific Ocean (e.g., Zhang 2005; Hsu and Li 2012). The MJO convection generates significant variations in large scale flow over the tropical and subtropical regions (e.g., Wang et al. 2013). Some observational and modeling studies have reported that in association with an eastward propagating MJO convection, the SSDs are usually suppressed ahead (i.e., east) of it and is enhanced within and west of it (e.g. Maloney 2009; Kiranmayi and Maloney 2011; Andersen and Kuang 2012). Such eddy activity anomaly is speculated to arise from barotropic conversion anomalies (e.g., Andersen and Kuang 2012). But several questions remain unclear. For instance, which component of environmental flow is critical for the barotropic conversion anomaly east and west of the MJO convection? Is the dominant process in the modulation of the MJO on the energetics of winter-time SSDs similar as that due to boreal summer ISO?

The present work aims to investigate the energetic balance of SSDs in the vicinity of MJO convection during boreal winter and tries to address the above questions. The rest of the paper is organized as follows. The data and methods used in the study are described in Sect. 2. Section 3 reveals the

relationship between the synoptic scale disturbances and the MJO envelope. Section 4 provides the energetic analysis to understand the dependence of synoptic scale disturbances on the MJO convection. Section 5 estimates the relative importance of the SSD upscale feedback to the MJO eastward propagation. The conclusion is given in Sect. 6.

## 2 Data and methods

### 2.1 Data

The datasets employed in this study include: (a) daily precipitation data from one degree daily (1DD) Global Precipitation Climatology Project (GPCP; Huffman et al. 2001) dataset, version 1.1; (b) daily atmospheric reanalysis data from ECMWF Interim Re-Analysis (ERA\_I; Dee et al. 2011). The three-dimensional fields from ERA\_I include zonal and meridional winds ( $u$  and  $v$ ), pressure velocity ( $\omega$ ), temperature ( $T$ ), specific humidity ( $q$ ), and geopotential ( $\phi$ ) at 19 levels from 1000 to 100 hPa with a 50-hPa interval. The analysis period for all the data spans from 1997 to 2008 during boreal winter (November to April) and all datasets are archived on a grid resolution of  $2.5^\circ$ .

### 2.2 Definition of synoptic scale disturbances

Previous studies on SSDs have used various definitions, in which the timescales of SSDs vary from 3 to 5 days (e.g., Wallace and Chang 1969) to 2.5–12 days (e.g., Maloney and Dickinson 2003) and to less than 30 days (e.g., Maloney 2009; Andersen and Kuang 2012). The results were not sensitive to various time scales. In this study, the SSD is defined as variations with a period of less than 20 days, as the intra-seasonal time scale is considered as 20–80 days.

### 2.3 Eddy kinetic energy budget

Following Hsu et al. (2011), a dependent variable could be separated into three components, the synoptic-scale field (below 20 days, denoted by a prime), the intraseasonal field (20–80 days, denoted by a tilde overbar) and the lower-frequency background state field (greater than 80 days, denoted by a double overbar):

$$A = \overline{\overline{A}} + \tilde{A} + A' \quad (1)$$

All the fields were obtained by using Lanczos band-pass filter (Duchon 1979) with a weight of 201. Then, the time change rate of eddy kinetic energy on the intraseasonal time scale may be derived as [or see Eq. 5 of Hsu et al. (2011)]

$$\frac{\partial \tilde{K}}{\partial t} = CK + CA + AM + FG \quad (2)$$

where

$$K = (u'^2 + v'^2)/2 \tag{3}$$

$$CK = -\mathbf{V}' \cdot \left[ \left( \overline{\overline{\mathbf{V}_3}} + \widetilde{\mathbf{V}_3} + \mathbf{V}'_3 \right) \cdot \nabla_3 \right] \overline{\overline{\mathbf{V}}} - \mathbf{V}' \cdot \left[ \left( \overline{\overline{\mathbf{V}_3}} + \widetilde{\mathbf{V}_3} + \mathbf{V}'_3 \right) \cdot \nabla_3 \right] \widetilde{\mathbf{V}} \tag{4}$$

$$CA = -\frac{R}{p} \overline{T' \omega'} \tag{5}$$

$$AM = -\overline{\overline{\mathbf{V}_3}} \cdot \nabla_3 K' - \widetilde{\mathbf{V}_3} \cdot \nabla_3 K' - \mathbf{V}'_3 \cdot \nabla_3 K' \tag{6}$$

$$FG = -\overline{\nabla_3 (\mathbf{V}'_3 \phi')} \tag{7}$$

Each budget term on the intraseasonal time scale was obtained by calculating regression against an MJO reference time series as described in Section 2d, and was denoted by a single overbar. *K* is the eddy kinetic energy (EKE). CK represents the barotropic conversion toward EKE from environmental flows, including both the lower-frequency background flow and intraseasonal flow. CA indicates the conversion from eddy available potential energy (EAPE) to EKE through a rising or sinking motion of warm or cold air parcels. AM represents the advection of EKE by the lower-frequency background flow, intraseasonal flow and synoptic flow. FG corresponds to the convergence of eddy geopotential fluxes. The subscript “3” means three dimensional. Note that only the CK and CA terms are real source (sink) of the EKE, while the other terms mainly represent the spatial redistribution of EKE (e.g., Maloney and Dickinson 2003).

### 2.4 Composite synoptic scale disturbances based on the MJO

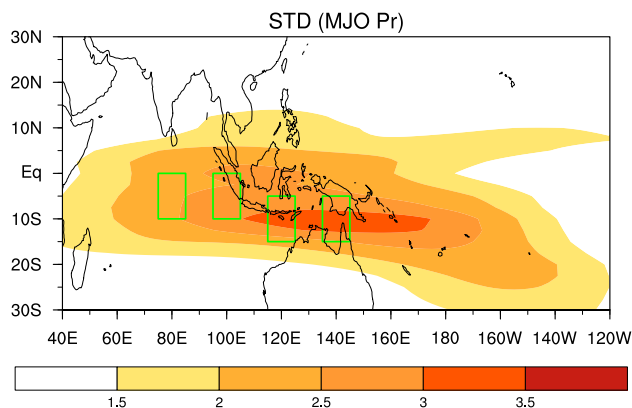
1. The raw precipitation (Pr) was filtered to the MJO spectral region (periods 20–80 day, eastward wavenumber 1–5) in the fashion of Wheeler and Kiladis (1999).
2. The standard deviation of the filtered Pr was calculated at each grid point and we identified the locations that have the largest magnitude. Figure 1 presents the horizontal distribution of the standard deviation of MJO Pr during boreal winter. Based on Fig. 1, four equally spaced reference boxes (10° × 10°) were selected; they cover the most active regions of MJO convection in the southern equatorial Indian Ocean and Pacific Ocean. Then, four MJO reference time series were constructed by box-averaged MJO Pr.
3. To look at the structure of a SSD field associated with the MJO convection, we regressed the SSD field onto each MJO reference time series. The regression coef-

ficients were multiplied by a typical MJO Pr anomaly (3 mm day<sup>-1</sup>) to give the magnitudes of the field anomalies associated with an MJO event.

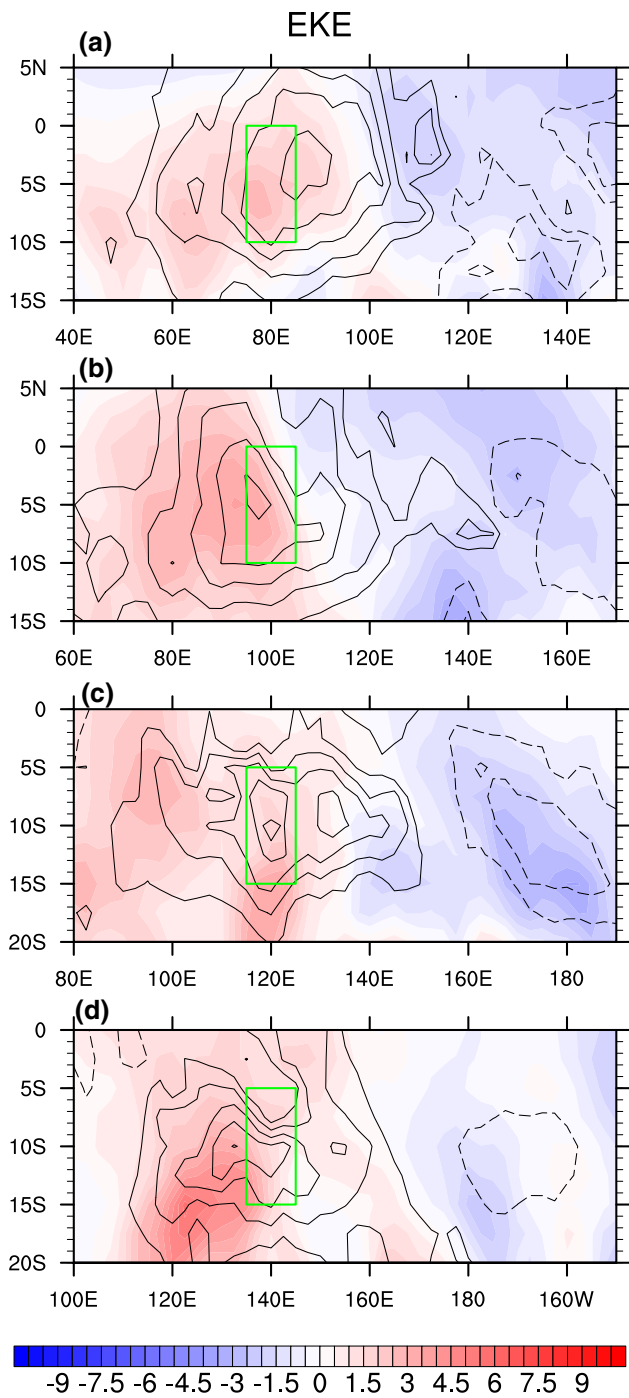
### 3 Characteristics of synoptic scale disturbances relative to MJO convection

Figure 2a–d display the horizontal distributions of MJO rainfall anomaly (contour) corresponding to the selected MJO rainfall time series; the shaded fields represent the intensity of SSD estimated by 1000–100 hPa averaged anomalous eddy kinetic energy. As expected, a large region of enhanced MJO rainfall anomaly is centered at the selected reference box in each panel (denoted by a green box), with a region of suppressed MJO rainfall anomaly to the east. Meanwhile, a zonal dipole structure of anomalous eddy kinetic energy is prominent in each panel, with a positive (negative) anomaly to the west (east). It shows that the SSD activity is enhanced within and to the west of the MJO convection center and is suppressed to the east of it.

Then, we examine the zonal-vertical structure of the eddy kinetic energy (shaded) averaged over -5° to +5° relative to the MJO center. For instance, for the MJO centered 80°E, 5°S, the band for average is 10°S–0°S. The contours represent the MJO zonal wind anomalies. Comparisons of Figs. 2 and 3 indicate that the column averaged zonal dipole structure of eddy kinetic energy anomaly shown in Fig. 2 is primarily contributed by the component in middle and lower troposphere (below 400 hPa).



**Fig. 1** Standard deviation of MJO Pr (shaded, units: mm day<sup>-1</sup>) in boreal winter (November–April). The green rectangles represent the selected MJO reference boxes. From left to right, they are (75°–85°E, 10°S–0°S), (95°–105°E, 10°S–0°S), (115°–125°E, 15°S–5°S) and (135°–145°E, 15°S–5°S)



**Fig. 2** Horizontal patterns of MJO rainfall anomalies (contours with an interval of  $1 \text{ mm day}^{-1}$ , negative values dashed) and eddy kinetic energy anomalies averaged over 1000–100 hPa (shaded, units:  $\text{m}^2 \text{ s}^{-2}$ ) relative to MJO convections from the eastern Indian Ocean to the Maritime Continent. The MJO reference box is indicated by a green box in each panel

Next, we examine the dominant structure of SSDs to the west and to the east of the MJO rainfall center, respectively. We begin by showing an example with the MJO rainfall center at  $80^\circ\text{E}$ . First, those days when the MJO rainfall

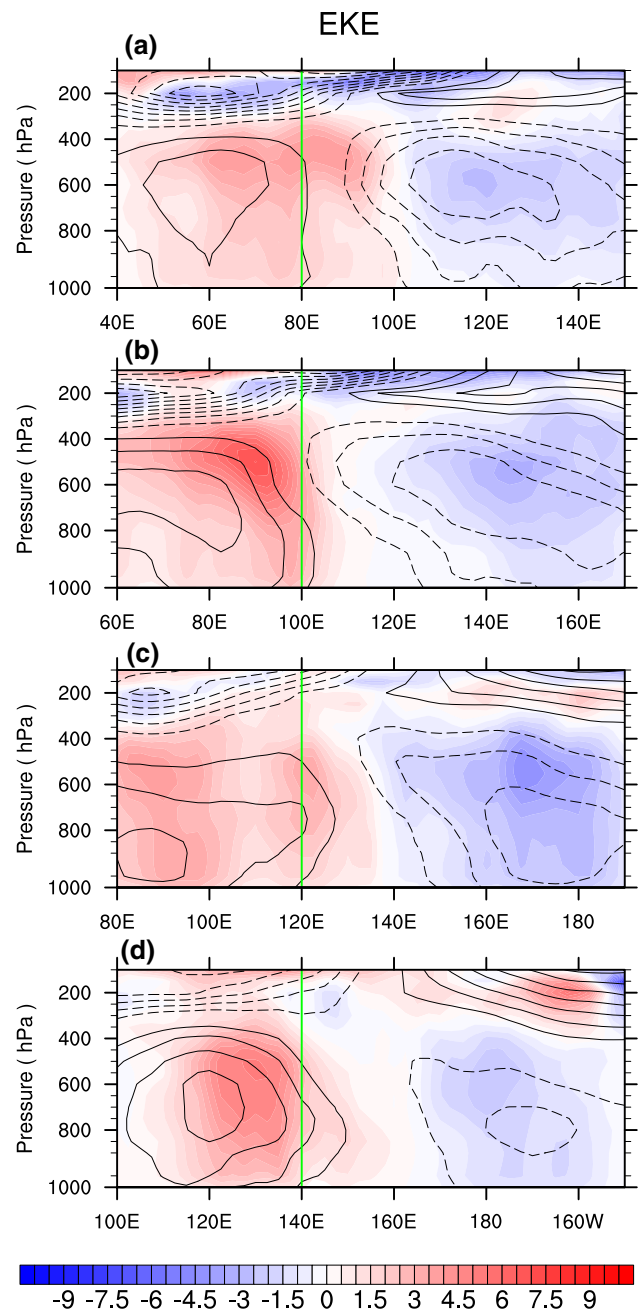


**Fig. 3** Longitude-vertical plots of MJO zonal wind anomalies (contours with an interval of  $0.5 \text{ m s}^{-1}$ , negative values dashed) and eddy kinetic energy anomalies (shaded, units:  $\text{m}^2 \text{ s}^{-2}$ ) relative to MJO convections from the eastern Indian Ocean to the Maritime Continent. The center of MJO convection is indicated by a green line in each panel. Each plot was obtained by the average over a  $10^\circ$  latitudinal band of the MJO reference box

time series exceeding one and a half standard deviation of itself are selected. Then, two time series of synoptic vorticity anomaly at 850 hPa are constructed by the selected days; one is at the base point  $70^\circ\text{E}, 5^\circ\text{S}$  while the other is at  $105^\circ\text{E}, 5^\circ\text{S}$ . Figure 4a (b) presents distribution

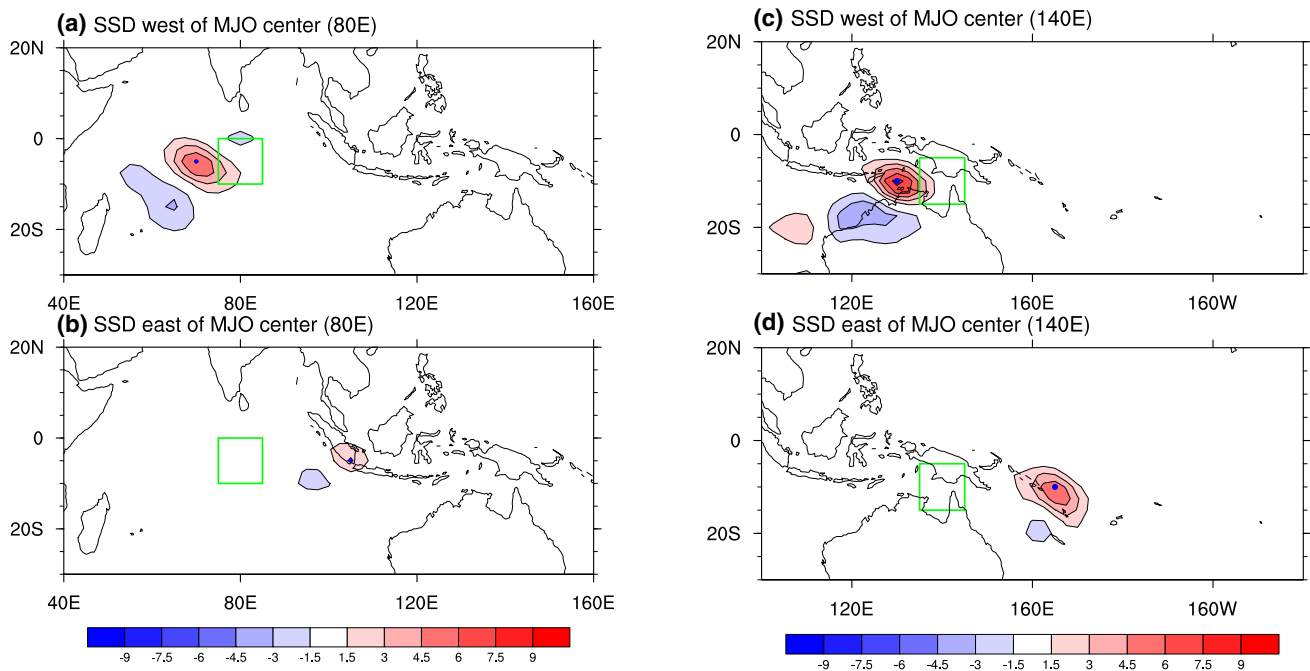


**Fig. 4** Horizontal structures of 850-hPa synoptic vorticity anomalies (units:  $10^{-6} \text{ s}^{-1}$ ) to the west or east of the MJO convection. The left (right) panels show results relative to the MJO convection centered at

80°E (140°E). The MJO convection center is marked by a green box in each panel, while the base point of synoptic disturbances is indicated by a solid dot

of regression coefficients between the 850-hPa synoptic vorticity anomaly of selected days at the west (east) base point and the corresponding fluctuations at all other grid points. The magnitude of regressed field is determined by the standard deviation of the synoptic vorticity time series. Comparisons between Fig. 4a, b reveal that the synoptic vorticity anomalies in the vicinity of the MJO rainfall center show a wavelike structure, with an apparent northwest to southeast tilt of the elongated extrema. However, the synoptic fluctuations are stronger to the west but weaker to the east. The contrasting amplitudes of the synoptic wave trains are consistent with the observed zonal dipole structure of the EKE anomalies as shown in Figs. 2 and 3.

The horizontal pattern of 850-hPa synoptic vorticity anomaly west (east) of the MJO convection at 140°E is displayed in Fig. 4c (d). It was calculated in a similar way as for the MJO convection at 80°E, except that the west (east) base point is 130°E, 10°S (165°E, 10°S). The northwest to southeast tilt of elongated extrema of synoptic vorticity anomalies is also prominent, and the contrasting amplitude of the wave train east and west of the MJO is also clear. Our calculation shows that such results are not sensitive to zonal locations of MJO rainfall center or the synoptic eddy base point (figures not shown).

It is worth mentioning that the northwest-southeast tilt of synoptic vorticity anomalies revealed from Fig. 4 are consistent with the dominant eddy structure in the southern

tropical region, because here the MJO base points are all south of the equator. In comparison, the dominant eddy structure in the northern tropical region during boreal summer shows a southwest-northeast tilt of elongated extrema (e.g., Lau and Lau 1990, Hsu et al. 2011).

#### 4 Energetic analysis of synoptic scale disturbances

To understand the zonal dipole structures of the SSD amplitude anomalies relative to the MJO convection, we analyze the kinetic energy balance in use of Eq. (2). Below, we only focus on CK and CA, because they are real source (sink) of the eddy kinetic energy while the other terms act to redistribute the EKE spatially. Since the results for all the four MJO reference locations are similar (see Figs. 2, 3), only those relative to MJO positive rainfall anomalies in the eastern Indian Ocean (centered at 80°E) and the Maritime Continent (centered at 140°E) are presented as a representative in the following.

The left and right panels of Fig. 5 display the horizontal patterns of 1000–100 hPa averaged CK and CA relative to MJO positive rainfall anomalies at 80°E and 140°E respectively. Both of them show positive anomaly to the west and negative anomaly to the east; the patterns agree well with the zonal dipole structure of column-averaged EKE anomalies



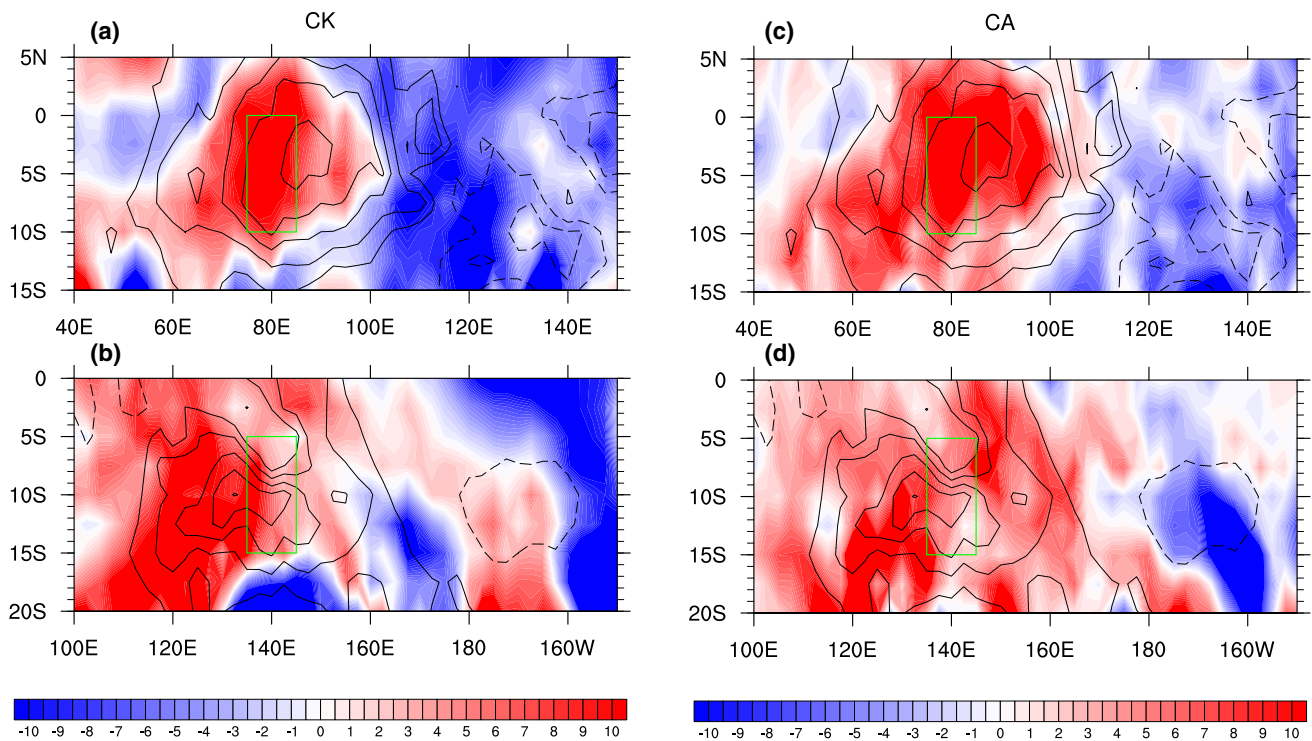


**Fig. 5** Same as Fig. 2, except that the shaded areas in the left (right) panels represent CK (CA) anomalies (units:  $10^{-6} \text{ m}^2 \text{ s}^{-3}$ ). The upper (lower) panels show results relative to the MJO convection centered at  $80^\circ\text{E}$  ( $140^\circ\text{E}$ )

shown in Fig. 2. Note that although some of the MJO reference centers are more off the equator than the others, the zonal dipole patterns of CK/CA look similar.

We further present the zonal-vertical structures of CK and CA, which were obtained from  $10^\circ$  latitude average near the reference centers (see Fig. 6). For all the reference locations,

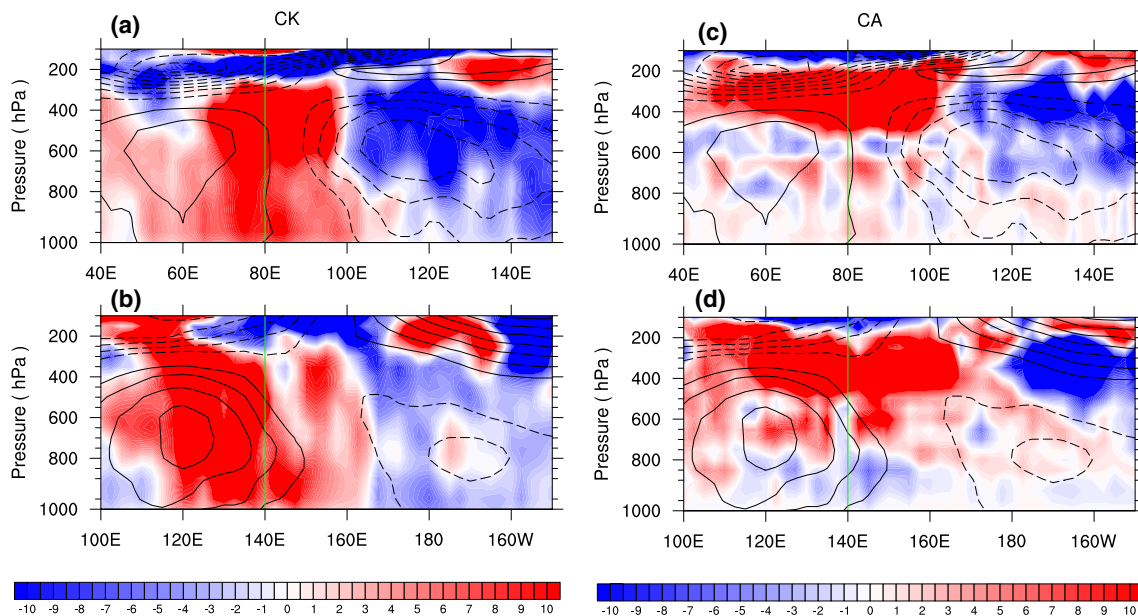


**Fig. 6** Same as Fig. 3, except that the shaded areas in the left (right) panels represent CK (CA) anomalies (units:  $10^{-6} \text{ m}^2 \text{ s}^{-3}$ ). The upper (lower) panels show results relative to the MJO convection centered at  $80^\circ\text{E}$  ( $140^\circ\text{E}$ )

the zonal dipole mode of CK is prominent below 300 hPa level while it of CA is mainly confined within 400–200 hPa level. Therefore, the column-averaged patterns of CK shown in Fig. 5 are primarily contributed by the component in middle and lower troposphere while the column-averaged patterns of CA are due to the component in upper troposphere. The sum of FG and AM act to redistribute the eddy kinetic energy generated by CK and CA vertically toward the highest level and boundary layer (figures not shown). To sum up, the enhanced EKE to the west is due to more barotropic energy conversion in middle and lower troposphere and more conversion of EAPE to EKE in upper troposphere, while the suppressed EKE to the east is due to less of them.

Then, what causes the more (less) generation of CK and CA to the west (east) of an MJO convection? We first look at the CK term. According to Eq. (4), CK could be further decomposed into 36 individual terms (or see Eq. 3 in Hsu et al. 2011) so that one could easily identify the dominant processes in the scale interactions among synoptic eddy, intraseasonal flow and lower-frequency background flow. After comparing the amplitude of each term, we finally identify four dominant contributors to the column-averaged CK anomaly; they are  $-\overline{u'^2 \frac{\partial \bar{u}}{\partial x}}$ ,  $-\overline{u'v' \frac{\partial \bar{u}}{\partial y}}$ ,  $-\overline{v'^2 \frac{\partial \bar{v}}{\partial y}}$  and  $\left(-\overline{u'v' \frac{\partial \bar{u}}{\partial y}}\right)$

(hereafter CK1, CK2, CK3 and CK4, respectively). The sum of the four terms account for 70% of the positive CK anomaly to the west and 50% of the negative CK anomaly to the east. Note that the first three terms reflect the influence of the intraseasonal flow on barotropic conversion and the last term indicates the role of lower-frequency background flow. Because the east–west asymmetry of CK anomalies mainly arise from lower and middle troposphere (see left panels of Fig. 6), in the following we will select 600 hPa level as a representative to investigate the horizontal patterns of the four primary CK terms and the associated environmental flows and understand their interactions.

Figure 7a, b present the horizontal patterns of CK1 at 600 hPa relative to MJO positive rainfall anomaly at 80°E and 140°E respectively. A positive anomaly is prominent near the MJO center in each panel. Since  $\overline{u'^2} > 0$ , the polarity of CK1 is determined by divergence of MJO zonal wind. As seen in Fig. 3, the MJO zonal wind anomalies are convergent near the MJO center in middle and lower troposphere and divergent in upper troposphere. The interaction between synoptic eddies and MJO zonal wind yields a local barotropic conversion from MJO to eddy kinetic energy near the MJO center in the middle and lower troposphere. This process was known as barotropic wave accumulation (Webster and Chang 1988; Holland 1995; Sobel and Bretherton 1999).

Figure 8a, b display the horizontal distributions of CK2 at 600 hPa (shaded) relative to MJO positive rainfall anomaly at 80°E and 140°E respectively. A zonal dipole structure of this term is apparent in each panel, with positive anomaly

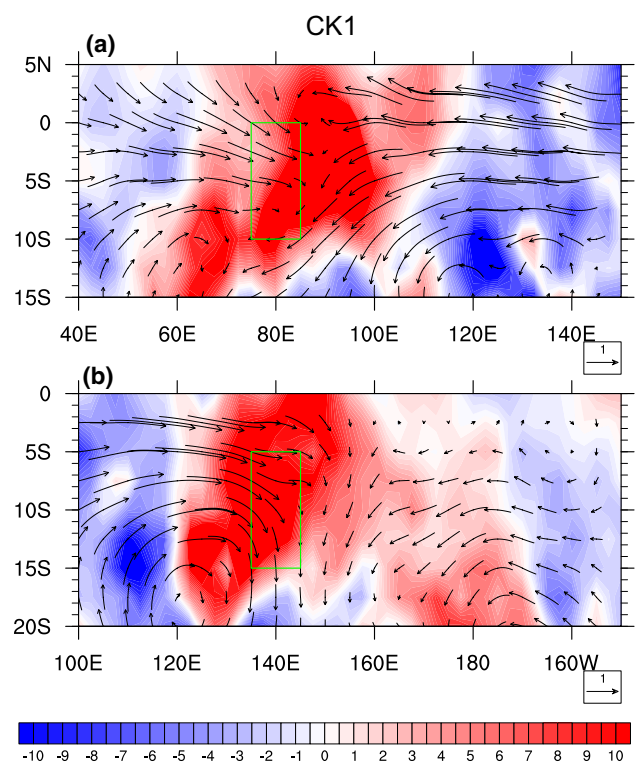


**Fig. 7** Horizontal distributions of 600-hPa MJO wind anomalies (vectors, units:  $\text{m s}^{-1}$ ) and CK1 (i.e.,  $-\overline{u'^2 \frac{\partial \bar{u}}{\partial x}}$ , shaded, units:  $10^{-6} \text{ m}^2 \text{ s}^{-3}$ ) relative to MJO convections centered at 80°E (a) and 140°E (b). The MJO reference box is indicated by a green box in each panel

to the west and negative anomaly to the east. Because the tilt structure of synoptic vorticity shown in Fig. 4 indicates a negative eddy momentum flux ( $\overline{u'v'} < 0$ ), the placement of synoptic disturbances in a region where the MJO zonal wind increases (decreases) with latitude implies a local barotropic conversion from MJO to eddy kinetic energy (eddy to MJO kinetic energy). As one can see, the MJO wind at 600 hPa (see vectors in Fig. 8a–d) is characterized by a cyclonic gyre to the west and an anticyclonic gyre to the east. They are related to the so-called “quadruple vortex structure” of the MJO (e.g., Zhang and Ling 2012), but the gyres south of the MJO base points are much more dominant while the gyres to the north are much weaker; this is due to that the MJO base points are all located south of the equator. Therefore, the equatorward gradient of MJO zonal wind is primarily positive (negative) to the east (west) of the MJO center, which gives rise to positive (negative) CK2 to the east (west).

The horizontal distributions of CK3 at 600 hPa relative to positive MJO rainfall anomaly at 80°E and 140°E are shown in Fig. 9a, b. They also show positive anomaly to the west and negative anomaly to the east in each panel, but the amplitudes are much weaker compared to CK2. Such zonal dipole patterns are due to interactions between synoptic eddies and meridional divergence of MJO wind. Since  $\overline{v'^2} > 0$ , the polarity of CK3 is determined by the divergence

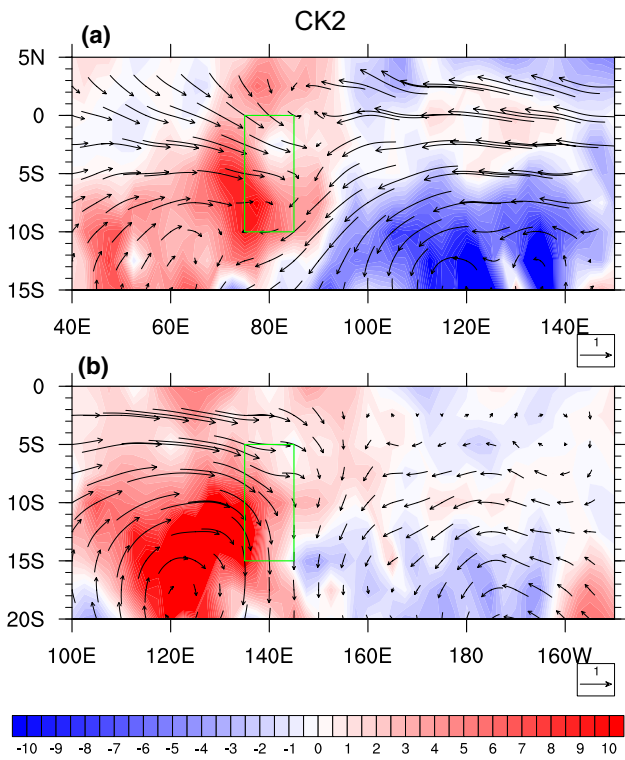


**Fig. 8** Same as Fig. 7, except that the shaded areas represent CK2 (i.e.,  $-u'v' \frac{\partial \bar{u}}{\partial y}$ )

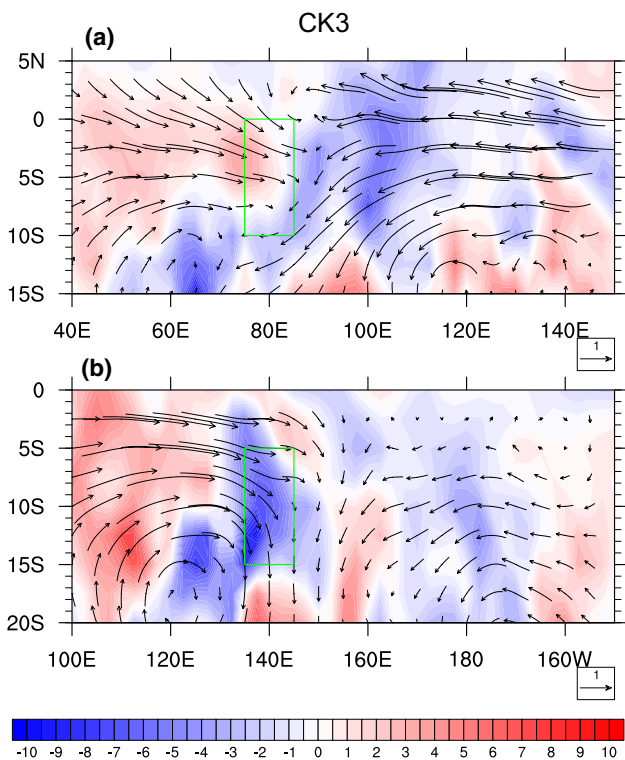


**Fig. 9** Same as Fig. 7, except that the shaded areas represent CK3 (i.e.,  $-v'^2 \frac{\partial \bar{v}}{\partial y}$ )

of MJO meridional wind. As shown by vectors in Fig. 9, the quadruple vortex structure of MJO generates meridional convergence (divergence) anomalies to the west (east).

Figure 10a, b present horizontal distributions of CK4 at 600 hPa. Significant positive anomalies of this term can be seen near and to the west of each MJO center, while weak negative anomalies are to the east. Figure 10c further presents boreal winter mean wind averaged at 600 hPa. As one can see, all the MJO centers are embedded in a large cyclonic gyre with positive meridional gradient of mean zonal wind (i.e.,  $\partial \bar{u} / \partial y > 0$ ). Therefore, stronger (weaker) barotropic conversion related to this term is possibly due to stronger (weaker) eddies themselves.

Next, we examine the variation of CA. Because CA anomalies mainly arise from the upper tropospheric component (see right panels of Fig. 6), in the following we only

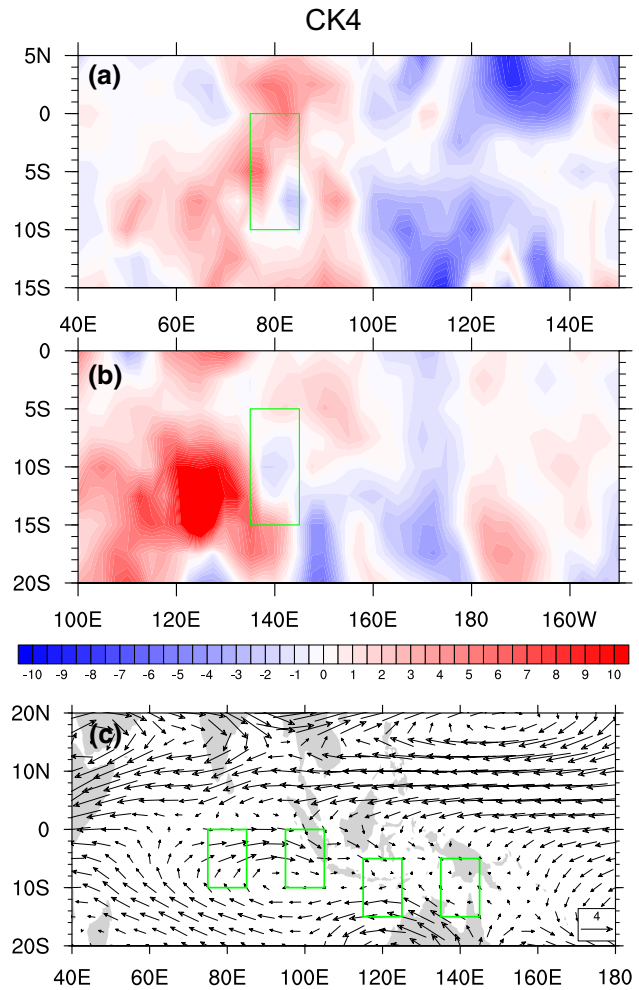


**Fig. 10** a, b Same as Fig. 7a, b, except for CK4 ( $-\overline{u'v' \frac{\partial \bar{u}}{\partial y}}$ ). c Horizontal pattern of 600-hP wind of boreal winter mean (vectors, units:  $\text{m s}^{-1}$ ). The green boxes denote the MJO reference boxes as shown in Fig. 1



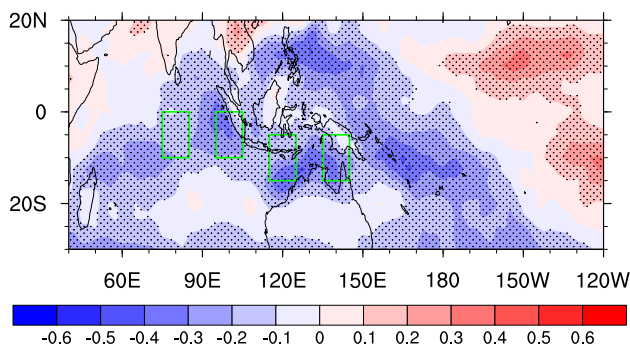


**Fig. 11** Correlation coefficients between vertical averaged (200–400 hPa) eddy temperature ( $T'$ ) and eddy pressure velocity ( $\omega'$ ) at each grid point during boreal winters in 1997–2008. Areas where the correlations are significant above the 95% confidence level are stippled. The green boxes denote the MJO reference boxes as shown in Fig. 1

focus on 200–400 hPa average. We first examine the coherent variation of eddy pressure velocity ( $\omega'$ ) and eddy temperature ( $T'$ ) in the upper troposphere where the conversion of EAPE is prominent. Figure 11 presents the correlation coefficients between  $\omega'$  and  $T'$  at each grid point during boreal winter. An out-of-phase relationship between  $T'$  and  $\omega'$  is prominent over the tropical Indian Ocean and western Pacific Ocean. It suggests that from long-term average point of view, the EAPE is converted toward EKE in the upper troposphere. Since the generation of EAPE in the upper troposphere is dominated by diabatic effects as external heating (cooling) is applied to warm (cold) air parcels (e.g., Lau and Lau 1992), we then examine the diabatic effects, as estimated by the product of eddy diabatic heating ( $Q'_1$ ) and eddy temperature ( $T'$ ) averaged over 200–400 hPa. Figure 12a, b display horizontal distributions of  $Q'_1 T'$  averaged over 200–400 hPa, obtained by regression against the MJO rainfall time series. It suggests that more (less) EAPE is generated to the west (east) through diabatic effects. Therefore, more (less) EAPE conversion to EKE to the west (east) is due to more (less) generated EAPE from diabatic effects.

### 5 Importance of synoptic scale disturbances to the MJO eastward propagation

One important upscale feedback exerted by the SSD on the MJO is through nonlinear moisture advection (e.g., Maloney 2009; Andersen and Kuang 2012; Nasuno et al. 2015). Figure 13a, b display the zonal-vertical distributions of intraseasonal moisture tendency ( $\frac{\partial \bar{q}}{\partial t}$ , contour) and nonlinear moisture advective tendency ( $-\nu' \frac{\partial q'}{\partial y}$ , shaded), obtained by regression against MJO reference time series at 80°E and 140°E respectively. The intraseasonal moisture tendency in each panel

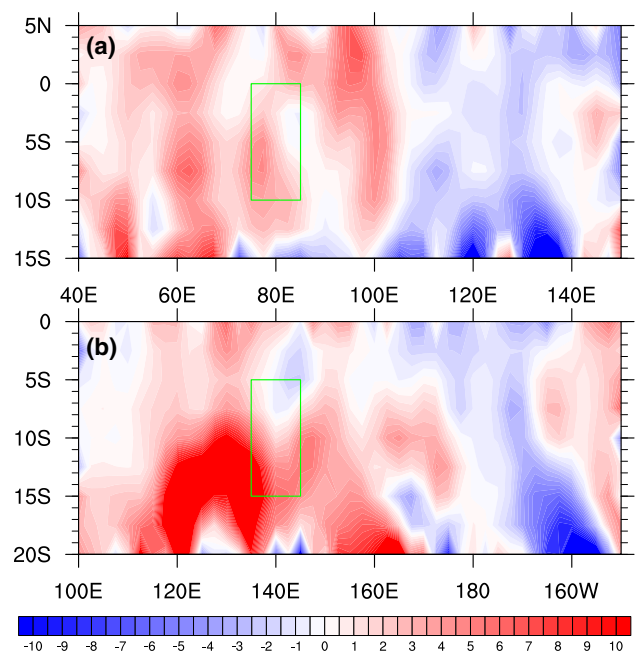


**Fig. 12** Horizontal distributions of product of eddy diabatic heating anomalies and eddy temperature anomalies ( $Q'_1 T'_1$ ) averaged over 200–400 hPa (shaded, units:  $10^{-7} \text{ m}^2 \text{ s}^{-3}$ ) relative to MJO convections centered at 80°E (a) and 140°E (b). The MJO reference box is indicated by a green box in each panel

exhibits a zonal dipole structure, with positive anomaly to the east and negative anomaly to the west. According to the moisture mode theory, such east–west asymmetry of intraseasonal moisture tendency relative to an MJO convection is critical in its eastward propagation (e.g., Sobel et al. 2014; Wang et al. 2017, 2018). Meanwhile, the nonlinear moisture advective tendency in each panel also shows a zonal dipole structure, with positive (negative) anomaly to the east (west), indicating its role in contributing to the eastward propagation. It is also noted that the nonlinear advective tendency presents prominent negative anomalies near the MJO convection center, which implies its damping effect on the MJO convection. The distribution of nonlinear advective tendency is due to that of the SSD amplitude (see Figs. 2, 3); because SSDs play a role in drying the tropical air through enhancing mixings, enhanced (suppressed) SSDs imply positive (negative) moisture advective tendency anomaly.

How much does the nonlinear moisture advective tendency contribute to the MJO eastward propagation? We estimate it by computing the percentage of the east–west asymmetry of nonlinear moisture advective tendency against that of intraseasonal moisture advective tendency. The asymmetry is calculated by the difference of an east column average and a west column average (east minus west). For the MJO centered at 80°E, 5°S, the east (west) column is 110°E–140°E, 10°S–0°S (40°E–70°E, 10°S–0°S). The columns relative to

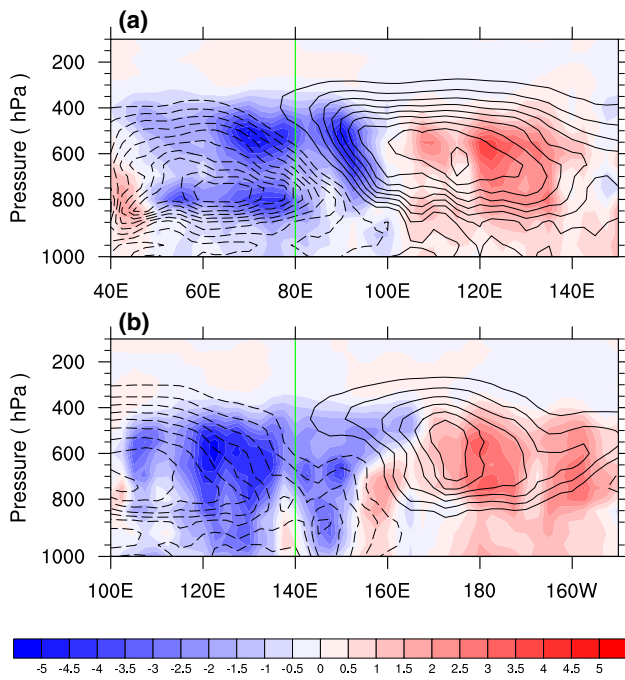


**Fig. 13** Longitude-vertical structures of moisture tendency ( $\frac{\partial \bar{q}}{\partial t}$ , contour interval is  $2 \times 10^{-10} \text{ s}^{-1}$  with negative values dashed) and nonlinear moisture advective tendency generated by synoptic disturbances ( $-v' \frac{\partial q'}{\partial y}$ , shaded, units:  $10^{-10} \text{ s}^{-1}$ ) relative to MJO convections centered at  $80^\circ\text{E}$  (a) and  $140^\circ\text{E}$  (b). The center of MJO convection is indicated by a green line in each panel

the other MJOs keep the same area, but change the locations with the change of MJO centers. The averaged percentage for the MJO at four locations is around 30%.

## 6 Summary

This study investigated the dependence of synoptic scale disturbances on the eastward propagating MJO convections in the southern equatorial regions during boreal winter with reanalysis data. It revealed that the synoptic scale disturbance is intensified within and to the west of the MJO convection and is weakened to the east of it. And the zonal dipole structure of the eddy kinetic energy anomaly is apparent through lower and middle troposphere. The dominant structure of the synoptic eddies to the west and east of the MJO convection is a wavelike disturbance, with an apparent northwest to southeast tilt of the elongated extrema of vorticity anomaly.

The energetic diagnosis revealed that the enhancement or suppression of the synoptic scale disturbance with the MJO convection is related to more or less barotropic conversion in the lower and middle troposphere and conversion of eddy available potential energy in the upper troposphere. There are

four dominant processes (accounted for 70%) in the barotropic conversion. The first process is due to barotropic wave accumulation (i.e.,  $-u'^2 \frac{\partial \bar{u}}{\partial x}$ ), which arises from zonal convergence of MJO flows in the lower troposphere at the convection center. The second process is related to the cyclonic (anticyclonic) circulation anomaly west (east) of the convection center (i.e.,  $-u'v' \frac{\partial \bar{u}}{\partial y}$ ), which is caused by meridional shear of MJO zonal flow. The third process is associated with the convergence (divergence) of MJO meridional wind anomaly west (east) of the MJO convection (i.e.,  $-v'^2 \frac{\partial \bar{v}}{\partial y}$ ). The fourth process (i.e.,  $-u'v' \frac{\partial \bar{u}}{\partial y}$ ) arises from the eddies intensities themselves, because the background flow is cyclonically sheared. More (less) conversion of eddy available potential energy to eddy kinetic energy to the west (east) of the MJO convection is due to more (less) generated eddy available potential energy from diabatic effects.

Furthermore, the zonal dipole pattern of synoptic-scale disturbance relative to the MJO convection benefit the MJO eastward propagation through generating zonal dipole mode of nonlinear moisture advective tendency. Our calculation indicates that around 30% of the east–west asymmetry of the intraseasonal moisture tendency is accounted for by that of the nonlinear moisture advective tendency.

It is known that most current state-of-art climate models have difficulty in simulating the eastward propagation of the MJO (e.g., Wang et al. 2017; Zhang et al. 2006), and the fundamental cause behind it has always been a research goal. Based on this study, the two-way interaction between the MJO's horizontal circulation pattern and the high-frequency eddy kinetic energy anomaly plays a role in the MJO eastward propagation. Then, a question arises as could the performance of models in simulating such two-way interaction explain the models' performance in the MJO eastward propagation? We will investigate this question in future study through multi-model results.

**Acknowledgements** LW was supported by NSFC 41705059 and the Startup Foundation for Introducing Talent of NUJST. LT was supported by National Key R&D Program 2017YFA0603802/2015CB453200, NSF AGS-1643297, NSFC 41630423, Jiangsu projects BK20150062 and R2014SCT00, and the Priority Academic Program Development of Jiangsu Higher Education Institutions (PAPD). This is SOEST contribution number 10456, IPRC contribution number 1344, and ESMC contribution 237.

## References

- Andersen JA, Kuang Z (2012) Moist static energy budget of MJO-like disturbances in the atmosphere of a zonally symmetric aquaplanet. *J Clim* 25:2782–2804. <https://doi.org/10.1175/jcli-d-11-00168.1>
- Bracken WE, Bosart LF (2000) The role of synoptic-scale flow during tropical cyclogenesis over the North Atlantic ocean. *Mon*

- Weather Rev 128:353–376. [https://doi.org/10.1175/1520-0493\(2000\)128%3C0353:TROSSF%3E2.0.CO;2](https://doi.org/10.1175/1520-0493(2000)128%3C0353:TROSSF%3E2.0.CO;2)
- Chang CP, Chen JM, Harr PA, Carr LE (1996) Northwestward-propagating wave patterns over the tropical western North Pacific during summer. *Mon Weather Rev* 124:2245–2266
- Chen L, Li T, Wang B, Wang L (2017) Formation mechanism for 2015/16 super El Niño. *Sci Rep* 7:2975. <https://doi.org/10.1038/s41598-017-02926-3>
- Dee DP, Uppala SM, Simmons AJ et al (2011) The ERA-Interim reanalysis: configuration and performance of the data assimilation system. *Q J R Meteorol Soc* 137:553–597. <https://doi.org/10.1002/qj.828>
- Duchon CE (1979) Lanczos filtering in one and two dimensions. *J Appl Meteorol* 18:1016–1022
- Holland GJ (1995) Scale interaction in the Western Pacific Monsoon. *Meteorol Atmos Phys* 56:57–79. <https://doi.org/10.1007/BF01022521>
- Hsu P-C, Li T (2012) Role of the boundary layer moisture asymmetry in causing the eastward propagation of the Madden–Julian oscillation\*. *J Clim* 25:4914–4931. <https://doi.org/10.1175/jcli-d-11-00310.1>
- Hsu P-C, Li T, Tsou C-H (2011) Interactions between boreal summer intraseasonal oscillations and synoptic-scale disturbances over the western North Pacific. Part I: energetics diagnosis\*. *J Clim* 24:927–941. <https://doi.org/10.1175/2010jcli3833.1>
- Huffman GJ, Adler RF, Morrissey MM, et al (2001) Global precipitation at one-degree daily resolution from multisatellite observations. *J Hydrometeorol* 2:36–50. [https://doi.org/10.1175/1525-7541\(2001\)002%3C0036:gpaodd%3E2.0.co;2](https://doi.org/10.1175/1525-7541(2001)002%3C0036:gpaodd%3E2.0.co;2)
- Kiranmayi L, Maloney ED (2011) Intraseasonal moist static energy budget in reanalysis data. *J Geophys Res Atmos* 116:D21117. <https://doi.org/10.1029/2011jd016031>
- Lau K-H, Lau N-C (1990) Observed structure and propagation characteristics of tropical summertime synoptic scale disturbances. *Mon Weather Rev* 118:1888–1913
- Lau K-H, Lau N-C (1992) The energetics and propagation dynamics of tropical summertime synoptic-scale disturbances. *Mon Weather Rev* 120:2523–2539. [https://doi.org/10.1175/1520-0493\(1992\)120%3C2523:TEAPDO%3E2.0.CO;2](https://doi.org/10.1175/1520-0493(1992)120%3C2523:TEAPDO%3E2.0.CO;2)
- Li T (2006) Origin of the summertime synoptic-scale wave train in the Western North Pacific\*. *J Atmos Sci* 63:1093–1102
- Li T (2014) Recent advance in understanding the dynamics of the Madden–Julian oscillation. *J Meteorol Res* 28:1–33. <https://doi.org/10.1007/s13351-014-3087-6>
- Li RCY, Zhou W, Li T (2013) Influences of the Pacific–Japan teleconnection pattern on synoptic-scale variability in the Western North Pacific. *J Clim* 27:140–154. <https://doi.org/10.1175/JCLI-D-13-00183.1>
- Liu F, Wang B (2012) Impacts of upscale heat and momentum transfer by moist Kelvin waves on the Madden–Julian oscillation: a theoretical model study. *Clim Dyn* 40:213–224. <https://doi.org/10.1007/s00382-011-1281-0>
- Liu F, Wang B, Kang I-S (2015) Roles of barotropic convective momentum transport in the intraseasonal oscillation. *J Clim* 28:4908–4920. <https://doi.org/10.1175/JCLI-D-14-00575.1>
- Maloney ED (2009) The moist static energy budget of a composite tropical intraseasonal oscillation in a climate model. *J Clim* 22:711–729. <https://doi.org/10.1175/2008JCLI2542.1>
- Maloney ED, Dickinson MJ (2003) The intraseasonal oscillation and the energetics of summertime tropical western North Pacific synoptic-scale disturbances. *J Atmos Sci* 60:2153–2168. [https://doi.org/10.1175/1520-0469\(2003\)060%3C2153:tioate%3E2.0.co;2](https://doi.org/10.1175/1520-0469(2003)060%3C2153:tioate%3E2.0.co;2)
- Maloney ED, Hartmann DL (2001) The Madden–Julian oscillation, barotropic dynamics, and North Pacific tropical cyclone formation. Part I: observations. *J Atmos Sci* 58:2545–2558. [https://doi.org/10.1175/1520-0469\(2001\)058%3C2545:tmjobd%3E2.0.co;2](https://doi.org/10.1175/1520-0469(2001)058%3C2545:tmjobd%3E2.0.co;2)
- McPhaden MJ (2004) Evolution of the 2002/03 El Niño\*. *Bull Am Meteorol Soc* 85:677–695. <https://doi.org/10.1175/BAMS-85-5-677>
- Nasuno T, Li T, Kikuchi K (2015) Moistening processes before the convective initiation of Madden–Julian oscillation events during the CINDY2011/DYNAMO period. *Mon Weather Rev* 143:622–643. <https://doi.org/10.1175/mwr-d-14-00132.1>
- Reed RJ, Recker EE (1971) Structure and properties of synoptic-scale wave disturbances in the equatorial Western Pacific. *J Atmos Sci* 28:1117–1133. [https://doi.org/10.1175/1520-0469\(1971\)028%3C1117:SAPOSS%3E2.0.CO;2](https://doi.org/10.1175/1520-0469(1971)028%3C1117:SAPOSS%3E2.0.CO;2)
- Seiki A, Takayabu YN (2007) Westerly Wind bursts and their relationship with intraseasonal variations and ENSO. Part II: energetics over the Western and Central Pacific. *Mon Weather Rev* 135:3346–3361. <https://doi.org/10.1175/mwr3503.1>
- Sobel AH, Bretherton CS (1999) Development of synoptic-scale disturbances over the summertime tropical northwest Pacific. *J Atmos Sci* 56:3106–3127
- Sobel A, Wang S, Kim D (2014) Moist static energy budget of the MJO during DYNAMO. *J Atmos Sci* 71:4276–4291. <https://doi.org/10.1175/jas-d-14-0052.1>
- Straub KH, Kiladis GN (2003) Interactions between the boreal summer intraseasonal oscillation and higher-frequency tropical wave activity. *Mon Weather Rev* 131:945–960. [https://doi.org/10.1175/1520-0493\(2003\)131%3C0945:ibtbsi%3E2.0.co;2](https://doi.org/10.1175/1520-0493(2003)131%3C0945:ibtbsi%3E2.0.co;2)
- Sui C-H, Lau K-M (1992) Multiscale Phenomena in the tropical atmosphere over the Western Pacific. *Mon Weather Rev* 120:407–430. [https://doi.org/10.1175/1520-0493\(1992\)120%3C0407:MPITT A%3E2.0.CO;2](https://doi.org/10.1175/1520-0493(1992)120%3C0407:MPITT A%3E2.0.CO;2)
- Wallace JM, Chang C-P (1969) Spectrum analysis of large-scale wave disturbances in the tropical lower troposphere. *J Atmos Sci* 26:1010–1025. [https://doi.org/10.1175/1520-0469\(1969\)026%3C1010:SAOLSW%3E2.0.CO;2](https://doi.org/10.1175/1520-0469(1969)026%3C1010:SAOLSW%3E2.0.CO;2)
- Wang L, Chen L (2016) Interannual variation of convectively-coupled equatorial waves and their association with environmental factors. *Dyn Atmos Oceans* 76(Part 1):116–126. <https://doi.org/10.1016/j.dynatmoce.2016.10.004>
- Wang L, Chen L (2017) Effect of basic state on seasonal variation of convectively coupled Rossby wave. *Dyn Atmos Oceans* 77:54–63. <https://doi.org/10.1016/j.dynatmoce.2016.11.002>
- Wang L, Li T, Zhou T, Rong X (2013) Origin of the intraseasonal variability over the North Pacific in boreal summer\*. *J Clim* 26:1211–1229. <https://doi.org/10.1175/jcli-d-11-00704.1>
- Wang L, Li T, Maloney E, Wang B (2017) Fundamental causes of propagating and non-propagating MJOs in MJOTF/GASS models. *J Clim* 30:3743–3769. <https://doi.org/10.1175/JCLI-D-16-0765.1>
- Wang L, Li T, Nasuno T (2018) Impact of rossby and kelvin wave components on MJO eastward propagation. *J Clim* 31:6913–6931. <https://doi.org/10.1175/JCLI-D-17-0749.1>
- Webster PJ, Chang H-R (1988) Equatorial energy accumulation and emanation regions: impacts of a zonally varying basic state. *J Atmos Sci* 45:803–829. [https://doi.org/10.1175/1520-0469\(1988\)045%3C0803:EEAER%3E2.0.CO;2](https://doi.org/10.1175/1520-0469(1988)045%3C0803:EEAER%3E2.0.CO;2)
- Wheeler M, Kiladis GN (1999) Convectively coupled equatorial waves: analysis of clouds and temperature in the wavenumber–frequency domain. *J Atmos Sci* 56:374–399. [https://doi.org/10.1175/1520-0469\(1999\)056%3C0374:ccewao%3E2.0.co;2](https://doi.org/10.1175/1520-0469(1999)056%3C0374:ccewao%3E2.0.co;2)
- Zhang C (2005) Madden–Julian Oscillation. *Rev Geophys* 43:RG2003
- Zhang C, Ling J (2012) Potential vorticity of the Madden–Julian oscillation. *J Atmos Sci* 69(1):65–78
- Zhang C, Dong M, Gualdi S et al (2006) Simulations of the Madden–Julian oscillation in four pairs of coupled and uncoupled global models. *Clim Dyn* 27:573–592. <https://doi.org/10.1007/s00382-006-0148-2>
- Zhou X, Wang B (2007) Transition from an eastern Pacific upper-level mixed Rossby-gravity wave to a western Pacific tropical cyclone. *Geophys Res Lett* 34:L24801. <https://doi.org/10.1029/2007GL031831>